Applied Physics A (2022) 128:895
https://doi.org/10.1007/s00339-022-06026-6

Applied Physics A
Materials Science & Processing

A comparative study of optical vanadium antimony borate glass doped with spinel ferrite using structural, spectral, and electrical measurements

A. M. A. Henaish[1,2] · **A. N. EL‑Sharkawy**[3] · **O. M. Hemeda**[1] · **R. Ghazy**[1] · **K. R. Mahmoud**[4] · **A. M. Dorgham**[5] · **M. M. Salem**[1] · **S. A. Abdel Gawad**[3]

Received: 25 June 2022 / Accepted: 3 September 2022 / Published online: 18 September 2022

Abstract

Recently glass composition with magnetic material nanoparticles has attracted a lot of interest by studying different compositions and ratios, which can be useful in controlling the composition's electrical, magnetic, and optical properties. In our study, borate oxide glasses were prepared using melt-quench technique with composition samples is (50-x) $B_2O_3 + 50\ Sb_2O_3 + x\ V_2O_5$ encoded into [BSV glass system] where $x = (0, 0.1, 0.2, 0.3, 0.4$ and 0.5 wt.%). Nickel ferrite was also prepared using Flash auto-combustion and mixed with the glass matrix to form a BSV composite glass system. These glasses were investigated by X-ray diffraction, transmission electron microscopic, different dielectric properties, and Fourier transform infrared. Further results show the cubic spinel structure of Nickel ferrite in XRD, and the particle size obtained from TEM images agrees with the size calculated from XRD at 25.52 nm. TEM of BSV glass system gives that the V_2O_5 nanoparticle was grown inside the borate glass matrix homogenous in the form of nanorods. It shows that the relaxation peaks shift toward lower frequency, and the conductivity increase by increasing vanadium oxide content in the BSV glass system. The ratio of the V_2O_5 content to the ferrite content determines the impact of ferrite addition to the glass matrix on the electrical properties. By comparing the dielectric constant for the same sample with and without ferrite, the dielectric properties increase for increased V_2O_5 concentration.

Keywords Borate glass · Vanadium oxide · Nickel ferrite · XRD · TEM · Dielectric properties · Cole Cole diagram · FTIR · DFT

1 Introduction

Glass–ceramics containing superparamagnetic, ferromagnetic, or ferrimagnetic materials have potential uses in several domains of electronic device manufacturing 1, 2. Electric devices, including low temperature cofired ceramics, electric modules, cathode ray tubes plasma, display panels, and multi-layer ceramic capacitors, have all benefited from the use of low melting glasses to reduce sintering temperatures and maximize coefficients of thermal expansion3, 4 The electrical, magnetic, and optical characteristics of glasses are profoundly affected by the presence of iron ions. Below the freezing point, individual spins are frozen in a random orientation due to antiferromagnetic interaction between neighboring ions, which is thought to be the general mechanism by which iron ions in glasses form clusters exhibiting superparamagnetic behavior5.

✉ A. M. A. Henaish
ahmed.henaish@science.tanta.edu.eg

[1] Physics Department, Faculty of Science, Tanta University, Tanta 31527, Egypt

[2] NANOTECH Center, Ural Federal University, Yekaterinburg 620002, Russia

[3] Physics Department, Faculty of Engineering, Misr University for Science and Technology, 6th of October City 12649, Egypt

[4] Physics Department, Faculty of Science, Kafr-Elsheikh University, Kafr-Elsheikh 33511, Egypt

[5] Basic Science Department, Higher Institute of Engineering and Technology, Tanta 31739, Egypt

Boron oxide is a good glass former since it makes a homogeneous formation of the glass matrix by interacting with different ratios of other oxides. The amorphous nature of borate glasses returns to the various networks formed in the presence of boron oxide (B_2O_3) in different arrangements of triangular BO3 and tetrahedral structural BO_4, $B3O_6$, or B_3O_7. Although antimony oxide has some crystal nature, boron oxide works as a good host and interacts well to form its glass matrix, and vanadium oxide help establish the amorphous nature of the glass. Antimony oxide (Sb_2O_3) is reported to have nonlinear optical properties since it has refractive index and transparent behavior in the glass matrix so it can be used in many glass applications. Sb_2O_3 structural units can be viewed as tetrahedral with form (Sb^{3+}) and can also exist in the Sb^{5+} state; this factor favors the glass formation 5–7. Vanadium oxide (V_2O_5) is one of the 3d transition metals, so it helps in giving several valences inside the glass matrix (V^{5+}, V^{4+}, and V^{3+}). This makes a good combination in borate glass since it prefers the high valence state oxides such as V_2O_5.

Ferrite is a compound with magnetic properties that can be used in different electronic industries and low coast materials. It was essential to compare glass and ferrite to investigate the effect of different results after and before adding ferrite to the glass matrix formation. Nickel ferrite (Ni Fe_2O_4) is an important soft ferrite material since it gives ferromagnetic properties, low conductivity, high resistance to current loss, and high electrochemical stability 4,8. The AC electrical properties can be enhanced with the addition of magnetic materials (ferrites) to the borate glass matrix, which is ascribed to the continual formation of conductive pathways in the glass network6, 7. Our study aims to synthesize the glass system doped with ferrite and study the interaction between ferrite and glass matrix overall the studied sample. This interaction can be explained in all analysis tools that all samples were performed. On the other hand, a correlation between pure ferrite phase, glass, and glass composite would benefit through light on the effect of ferrite doping in the glass matrix.

2 Experimental procedures

2.1 Preparation of borate antimony vanadium (BSV) glass system

The initial BSV glass system was obtained using the melt and quench (melting followed by casting the required samples) method from high purity oxides. The synthesis of BSV can be described by the following:

$$(0.5 - x)\ \text{wt.\%}\ B_2O_3 + (0.5)\ \text{wt.\%}\ Sb_2O_3 + (x)\ \text{wt.\%}\ V_2O_5$$

where $x = 0, 0.1, 0.2, 0.3, 0.4, 0.5$ wt.%. The mixed weights give a homogeneous mixture, finely ground and placed in a porcelain crucible held in a furnace at 800 °C for about 20 min. After melting, the prepared glass was suddenly quenched at 100 °C using a stainless-steel plate and formed approximately a disk shape, as shown in Fig. 1.

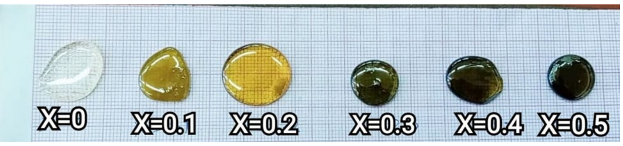

Fig. 1 HYPERLINK "sps:id::fig1||locator::gr1||MediaObject::0" The prepared BSV glass system

Fig. 2 The prepared BSV/$NiFe_2O_4$ composite glass system

2.2 *Preparation of $NiFe_2O_4$ nanoparticles*

The Flash auto-combustion method was used to synthesize $NiFe_2O_4$ nanoparticles. The raw materials used in the synthesis of these nanoparticles were nickel nitrate [$Ni(NO_3)_2.6H_2O$], iron nitrate [$Fe(NO_3)_3.9H_2O$], and urea [$CO(NH_2)_2$] as a fuel. The materials were continuously stirred for a few minutes with a magnetic stirrer and then heated, on a hot plate, at 80 °C for 30 min. In the end, the original solution changed into a viscous solution. Internal ignition occurred, and a brown ferrite powder was finally formed. The as-prepared powder was annealed for 4 h at 600 °C to eliminate the crystal strain and lattice defects to avoid any external phases.

2.3 *Preparation of BSV/$NiFe_2O_4$ composite system*

BSV/$NiFe_2O_4$ composite system was obtained using the melt and quench method with a chemical composition of (0.5-x) wt.% B_2O_3 + (0.5) wt.% Sb_2O_3 + (x) wt.% V_2O_5 where x = (0.1, 0.3 and 0.5) wt.% doped with a constant value of nickel ferrite in a powder form (0.05 gm, i.e., 0.3% from the combined weight to keep the glass in a transparent shape). The weighted precursors were mixed to get a uniform compositional mixture and finely ground taken in porcelain crucibles kept inside the electric furnace for melting. The glass blends were maintained at a temperature of 800 °C for about 20 min. The prepared glasses were suddenly molded at 100 °C using a stainless-steel plate to take shape in discs form, as shown in Fig. 2.

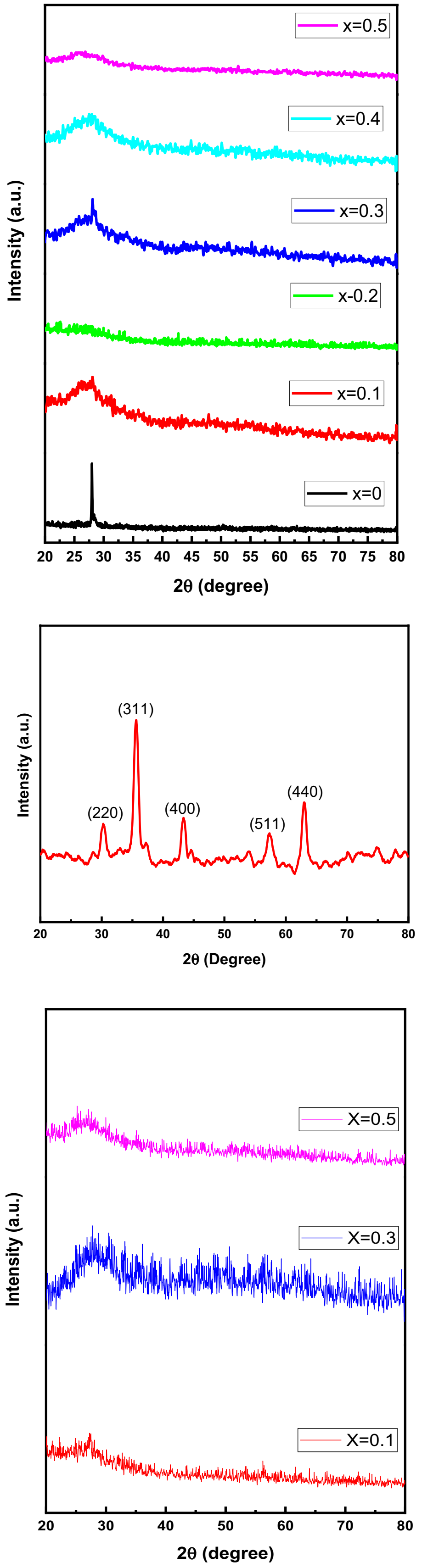

Fig. 3 **1** The XRD pattern of the BSV glass system with different V_2O_5 concentrations. **2** XRD of $NiFe_2O_4$ annealed at 800 °C. **3** XRD of BSV/$NiFe_2O_4$ glass composite

2.4 Sample structure, morphology, optical and electrical properties

The amorphous character of prepared glasses and $NiFe_2O_4$ were confirmed using the X-ray diffraction (XRD) technique with Cu Kα radiation source ($\lambda = 1.54$ nm) Philips model (PW-1729) step size 0.02 °C; time per step is 21 s (Research Center, Cairo). The optical properties of the samples were also characterized using Fourier transform Infrared (FTIR) spectrometer using a PERKIN-ELMER-1430 recording infrared spectra in the range of 200 to 4000 cm^{-1}. Transmission electron microscope (TEM) image analysis was performed in a JEOL-JEM-2100 operated at 200 kV (Research Center, Cairo). The samples morphology was investigated using a scanning electron microscope-SEM (JOEL, Model: JSM-5600, Japan) equipped with a secondary electron detector (Research Center, Cairo). Electrical parameters such as AC conductivity, dielectric loss, permittivity, electric modulus, impedance, and dissipation factor (tan δ) were analyzed using Novocontrol concept 40 broadband dielectric spectrometers (BDS) with high accuracy Alpha impedance analyzer from 0.1 Hz to 20 MHz (Research Center, Cairo).

3 Results and discussion

3.1 X-ray diffraction (XRD)

3.1.1 XRD for BSV glass system

XRD studies the phases of crystallization and amorphous nature of different samples. Figure 3.1 show an amorphous crystalline nature of the BSV glass system (0.5-x) wt.% B_2O_3 + (0.5) wt.% Sb_2O_3 + (x) wt.% V_2O_5 where x = (0, 0.1,0.2, 0.3, 0.4 and 0.5) wt.% In this glass system contains antimony oxide, which is known as a weak glass network former but not in the presence of glass modifiers like B_2O_3 and $V_2O_5$8. As shown in Fig. 3, the BSV that doesn't contain V_2O_5 shows a sharp peak at around 28.02°; this is due to the presence of well-defined randomly distributed crystal nature in a glass matrix return to the presence of Sb_2O_3 (antimony oxide)8. Vanadium oxide (V_2O_5) is a good glass modifier, so it helps to increase the non-crystalline (amorphous) nature of the glass by helping decrease the sharp peak found at sample BSV ($x = 0$) by increasing of V_2O_5 content gradually. This means that V_2O_5 increases the amorphous nature of the BSV glass system due to the formation of the glass matrix. There are no other sharp peaks in the BSV glass system, which clear the amorphous and non-crystalline nature of the glass matrix.

3.1.2 XRD of $NiFe_2O_4$ nanoparticles

The diffraction pattern of the ferrite sample ($NiFe_2$ O_4) is shown in Fig. 3.2, which is annealed at 800 °C. It exhibits the diffraction grains (220), (311), (400), (511), and (440), indicating the presence of cubic spinel structure of Nickel ferrite. The strong and high intensity of the peaks indicates the high crystallinity of the material. The phase purity was ensured in the absence of any foreign phases.

The average crystallite size is obtained using the Debye Scherrer equation9:

$$D = \frac{0.9\lambda}{\beta_{hkl}\cos\theta} \tag{1}$$

where β_{hkl} is full width at half the maximum of the diffraction peak, λ is the wavelength of X-ray 1.541 Å, and θ is Bragg angle.

The lattice parameter of the cubic $NiFe_2O_4$ sample was calculated using the relation10:

$$a = d_{hkl}\sqrt{h^2 + k^2 + l^2} \tag{2}$$

where d_{hkl} is the interplanar distance and (hkl) are miller indices of each plan.

The average value of lattice parameter and crystallite size were 8.436 °A and 25.6 nm, respectively, which matches the same ferrite sample in the literature11.

3.1.3 XRD of BSV/$NiFe_2O_4$ glass composite

XRD analysis focuses on studying different glass samples' crystallization and amorphous nature. XRD of (0.5-x) wt.% B_2O_3 + (0.5) wt.% Sb_2O_3 + (x) wt.% V_2O_5 where x = (0.1, 0.3 and 0.5) wt.% doped with fixed ratio 0.05 gm of nickel ferrite encoded into BSV/ferrite glass composite shown in Fig. 3.3. The XRD spectra shown in Fig. 3.3 confirmed the uncrystallized solid (amorphous nature) of these glass /ferrite composites 12. The XRD pattern of borate glass exhibited broad diffusion at $2\Theta = 27°$; this indicates the presence of long-range structure disorder and confirms the amorphous nature instead of crystalline peaks12, 13. Although XRD of nickel ferrite exhibit a cubic spinel structure but the presence of B_2O_3 and V_2O_5 modifier help to overcome the amorphous nature of the glass/ferrite composite14. B_2O_3 and V_2O_5 are good glass modifiers, and their presence of them both support the amorphous nature of BSV/ ferrite composite15.

3.2 FTIR analysis

3.2.1 FTIR of BSV glass system

FTIR spectra shown in Fig. 4 provide different functional group information about interaction between different content in the glass matrix according to the Eq. (50-x) B_2O_3 + 50 Sb_2O_3 + x V_2O_5 where x = 0, 0.1, 0.2, 0.3, 0.4 and 0.5. The assignment of different peak positions of FTIR bands is found in Table 1. The broad band at approximately 3435–3459 cm^{-1} corresponds to the symmetric O‒H stretching of H_2O. It shifts to a higher wavelength with increasing V_2O_5 content. The remaining bands related to boron, vanadium, and antimony mean that all metal oxide contributes to the glass matrix formation. The band of approximately 1617–1641 cm^{-1} comes from the vibration of B–O in the BO_3 group, whereas the band at 1189–1224 is due to the BO_4 group. Both bands shift to a lower wavelength by increasing vanadium oxide content. The band arises at 1059–1082 cm^{-1} from stretching V–O–V and V=O double

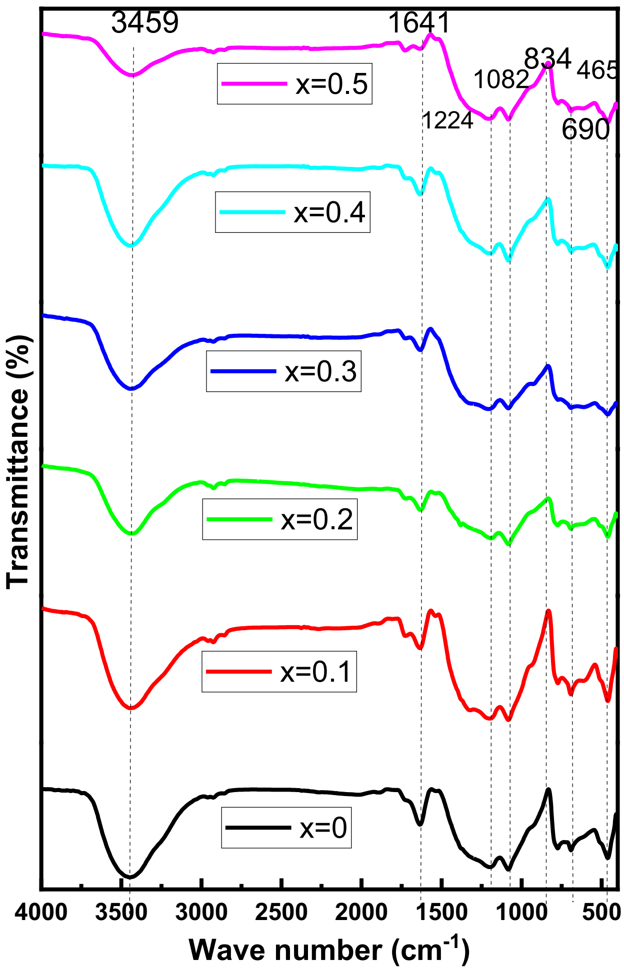

Fig. 4 FTIR spectra of BSV glass system

Table 1 different peak positions with different V_2O_5 content in the BSV glass system

X	Antimony oxide (metal cations)	O–B–O and V=O	B–O–B and B–O–V–O–B bridge	V=O double bond	BO_4 group	BO_3	OH group or stretching due to molecular water
0	453	690	834	1082	1224	1641	3447
0.1	465	690	834	1082	1201	1629	3435
0.2	465	690	834	1070	1189	1641	3435
0.3	465	678	834	1059	1213	1617	3459
0.4	465	678	834	1059	1213	1617	3459
0.5	465	678	834	1059	1213	1617	3459
Refs	[6, 17]	[18, 19]	[18, 20]	[21, 22]	[22]	[22, 23]	[24]

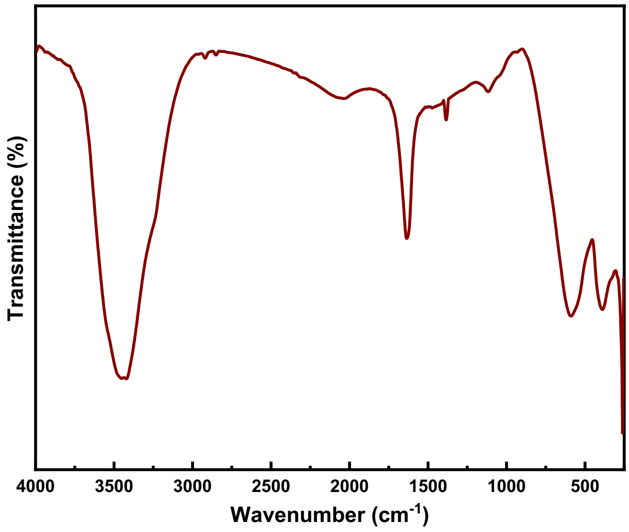

Fig. 5 FTIR analysis of Nickel ferrite

bond, and the band at 834 comes from the formation of stretching band B–O–B and B–O–V–O–B bridge. The band at 678–690 cm^{-1} assign to O–B–O and V=O double bond, so it made like deformation and bending mode of borate units. Finally, at 453–465 cm^{-1} reflect, the metal–oxygen bond Sb^{3+}–O^{2-} as shown in literature, is related to the antimony group16.

3.2.2 FTIR of nickel ferrite

The infrared spectra of $NiFe_2O_4$ in the range of 200–4000 cm^{-1} is shown in Fig. 5. The prominent characteristic absorption bands of ferrite are the tetrahedral absorption band around 589 $cm^{-1}$and the other absorption band for the octahedral site around 386 cm^{-1}. The absorption spectra are produced from the vibration of the Fe^{3+}–O^{2-} bond at both octahedral and tetrahedral sites. The presence of the two absorption bands at the different positions because the length of these bonds is different in the case of octahedral and tetrahedral sites. The mode of vibration of the two bands is stretching vibration [10, 25–27]. Similar results were reported for the Nickel ferrite sample synthesized through the flash method was urea has taken as fuel28. The band appearing at 3422 cm^{-1} is due to the symmetric vibration of the OH group, whereas the band appearing at 1116 cm^{-1} is due to the O–H bending vibration. The small band

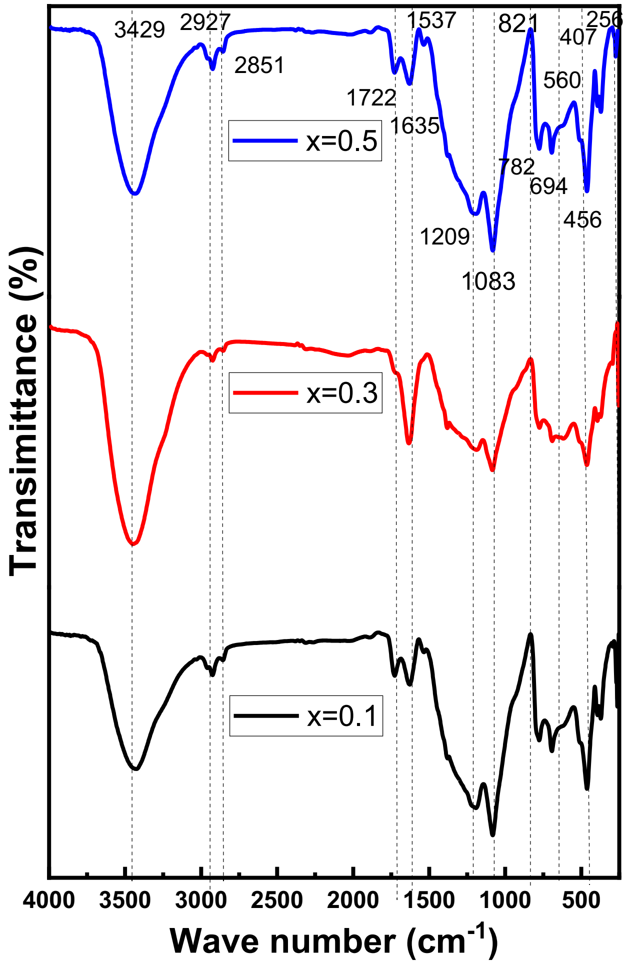

Fig. 6 FTIR spectra of BSV glass system composite with nickel ferrite

Table 2 The absorption band positions obtained from FTIR spectra

Sample	0.1	0.3	0.5	Assignment	References
A	368	368	368	Octahedral absorption band of Fe^{3+}–O^{2-}	[6, 18]
B	456	469	456	Vibration of Fe–O bond in tetrahedral site	[6, 24, 30]
C	694	694	694	Bending vibration B–O–B bonds and Vs=O bond	[6, 31]
D	782	782	782	Stretching vibration of B–O bond in Bo_4 group	[6, 17, 18]
E	1083	1070	1083	V=O double bond	[31]
F	1209	1209	1209	Symmetric stretching in Bo_3 units from pyro and Orth-borate groups and Bo_4 group	[30, 31]
G	–	1396	–	Asymmetric stretching of B–O of trigonal Bo_3	[18, 23]
H	1635	1635	1635	Combination of relaxation of B–O band of trigonal Bo_3 units in a glass matrix and C=O in ferrite	[23]
I	2851	2851	2851	Hydrogen bonding	[19, 20]
J	2927	2927	2927	Hydrogen bonding	[6]
K	3453	3440	3429	Molecular water	[6]

appearing at 2300 cm^{-1} was attributed to the free absorbed water's H–O–H bending vibration. The absorption band at 1635 cm^{-1} is attributed to the stretching vibration of the C=O. The last absorption band at 1384 cm^{-1} is attributed to the bending vibration CH.

Finally, the FTIR spectra can illustrate the molecular structure of the synthesized Nickel ferrite and study the different bonds in the given sample.

The force constant was estimated from the equation[29]:

$$F = 4\pi^2 C^2 \upsilon^2 \mu \tag{8}$$

where F is the force constant in dyne/cm, C is the speed of sound, υ is wavenumber in cm^{-1}, μ is reduced mass and was given by 2.2067×10^6 (dyne/cm), with the value agreeing with that published in the previous work[28].

Table 3 The detected functional group of the BSV glass system using IR analyze-RAMalyzeTrial.lic software

Vibration	Start wavenumber	End wavenumber
C–H bend, CH_2 /CH_3	1470	1445
C–H bend, alpha CH_2	1210	1190
C–C Skeletal	1130	1105
C–C=O, C–C stretch	960	910
X–C=O def	540	460

3.2.3 FTIR of BSV/$NiFe_2O_4$ composite glass system

The FTIR spectra of BSV glass composite doped with ferrite are shown in Fig. 6 for different V_2O_5 and the constant ratio of nickel ferrite. The spectra show a similar functional group as the BSV glass system in addition to the two characteristic

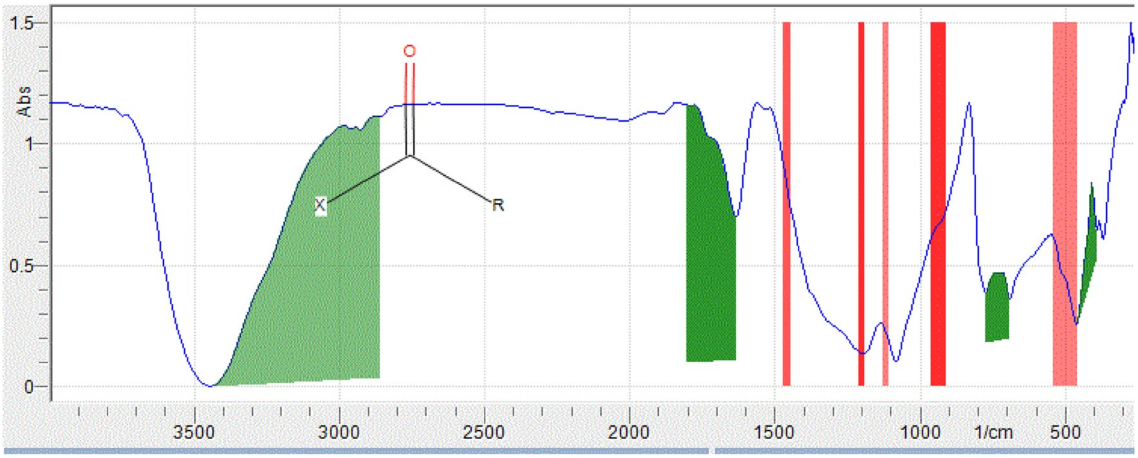

Fig. 7 The detected functional group of the BSV glass system using IR analyze-RAMalyze Lic software

Table 4 The detected functional group of BSV glass system using IR analyze-RAMalyzeTrial.lic software

Vibration	Start wavenumber	End wavenumber
C=O stretch	1850	1750
C–H stretch	3090	2855

bands that appeared in the far infrared region, which were assigned to octahedral and tetrahedral group complex for Fe $^{3+}$–O^{2-}. The absorption bands that appear in Fig. 6 are summarized in Table 2.

Using IR analyze-RA Malyze Lic software, the functional group was detected for the BSV glass system. The BSV composite glass system is shown in Fig. 7.

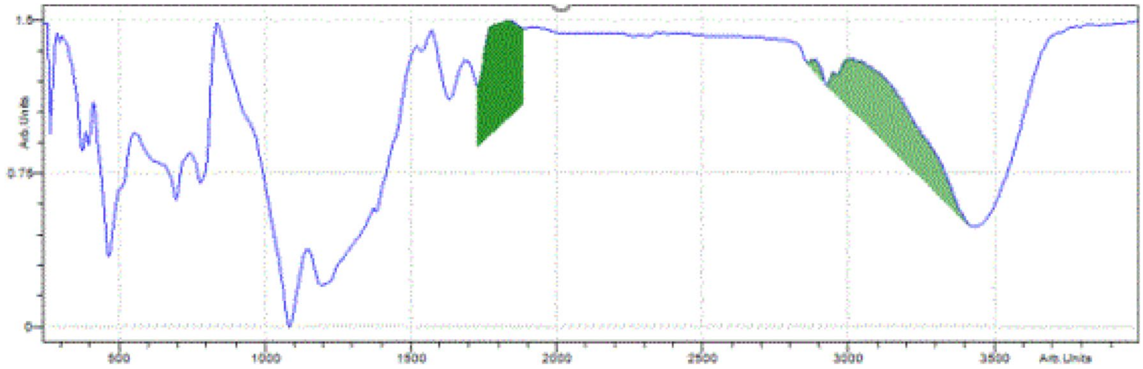

Fig. 8 The detected functional group of BSV glass system using IR analyze-RAMalyze Lic software

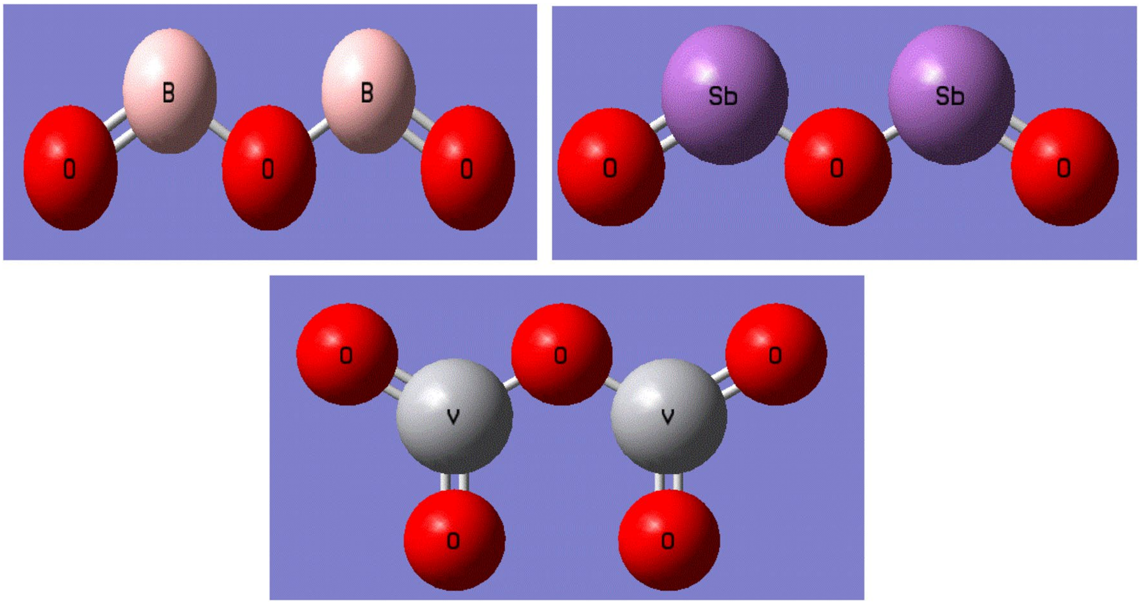

Fig. 9 Fram work of connection between boron oxide B_2O_3, Sb_2O_3 and V_2O_5

Table 5 Deduced IR spectra from DFT

Theoretical peak		Experimental peak	
424	Interact between B_2O_3 and Sb_2O_3	424	Antimony oxide (metal cations)
1301, 2239	Due to B_2O_3 in the form of BO_3 and BO_4	1301, 2239	–
3349	From V_2O_5	3349	OH group or water
3497, 3962	Interaction between V_2O_5 and Sb_2O_5	3497, 3962	–

As given from the program data, additional bands are detected and predicted at frequency regions that don't appear in the experimental one and are given in Table 3 for the pure glass system at $x = 0.3$ V_2O_5.

The same results for the BSV ferrite composite system are shown in Fig. 8, and the predicted bands are given in Table 4.

Density function theory (DFT):

The theoretical methodology (DFT) describes the frame work of connection between boron oxide B_2O_3, Sb_2O_3, and V_2O_5 as shown in Fig. 9. All measurements were calculated using Gaussian 09 software within the DFT system as given in Table 5. the glass system was designed using Ground State DFT B3LYP Basic Set STO-3G software. Figure 10 shows FTIR and calculated infrared spectra that show a new band not found in the experimental data. The FTIR spectra for the completed interaction between B_2O_3, Sb_2O_3, and V_2O_5 to form the glass system are shown in Fig. 11.

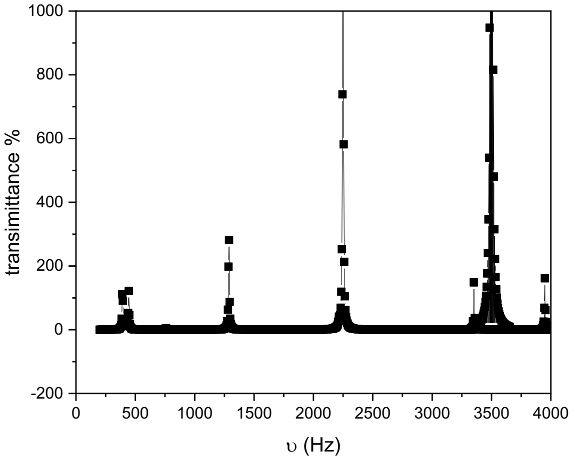

Fig. 11 The FTIR spectra for the completed interaction between B_2O_3, Sb_2O_3, and V_2O_5 to form the glass system

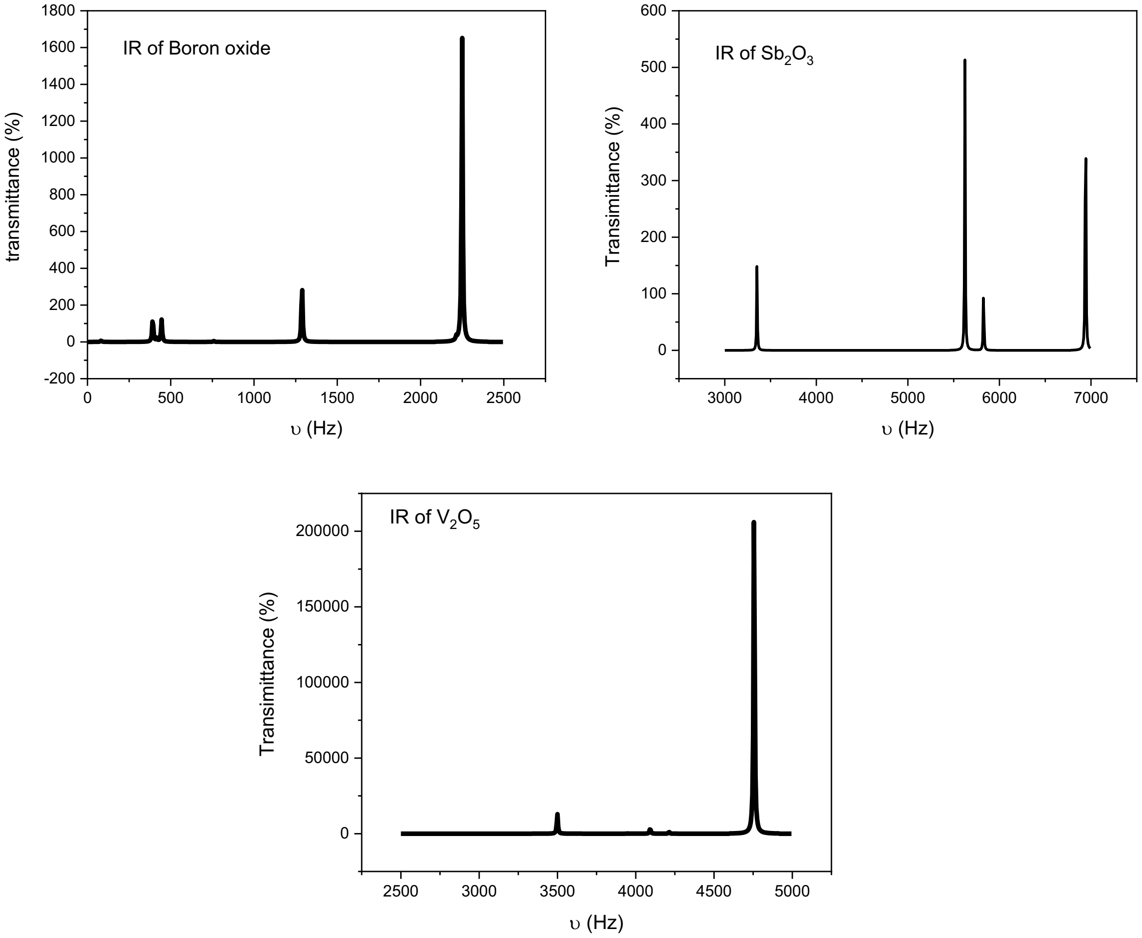

Fig. 10 Calculated infrared spectra of B_2O_3, Sb_2O_3, and V_2O_5

3.3 TEM

3.3.1 TEM of BSV glass system

TEM (transmission electron microscope) micrographs for BSV glass sample containing 0.1, 0.3 and 0.5 V_2O_5 wt.% are illustrated in Fig. 12. It was observed that the V_2O_5 nanoparticle was grown inside the borate glass matrix homogenous in the form of nanorods with a diameter, as shown in Table 6 (Fig. 13).

The diameter of the nanorod increases by increasing V_2O_5 content from 41.57 to 76.67 nm for $x = 0.1$ and $x = 0.5$, respectively, indicating the growth of the V_2O_5 nanorod by increasing its content. The structure of the nanorod is a solid rod with a closed end. The rolling of the V_2O_5 layer form the nanorods. The TEM results show a typical structure without

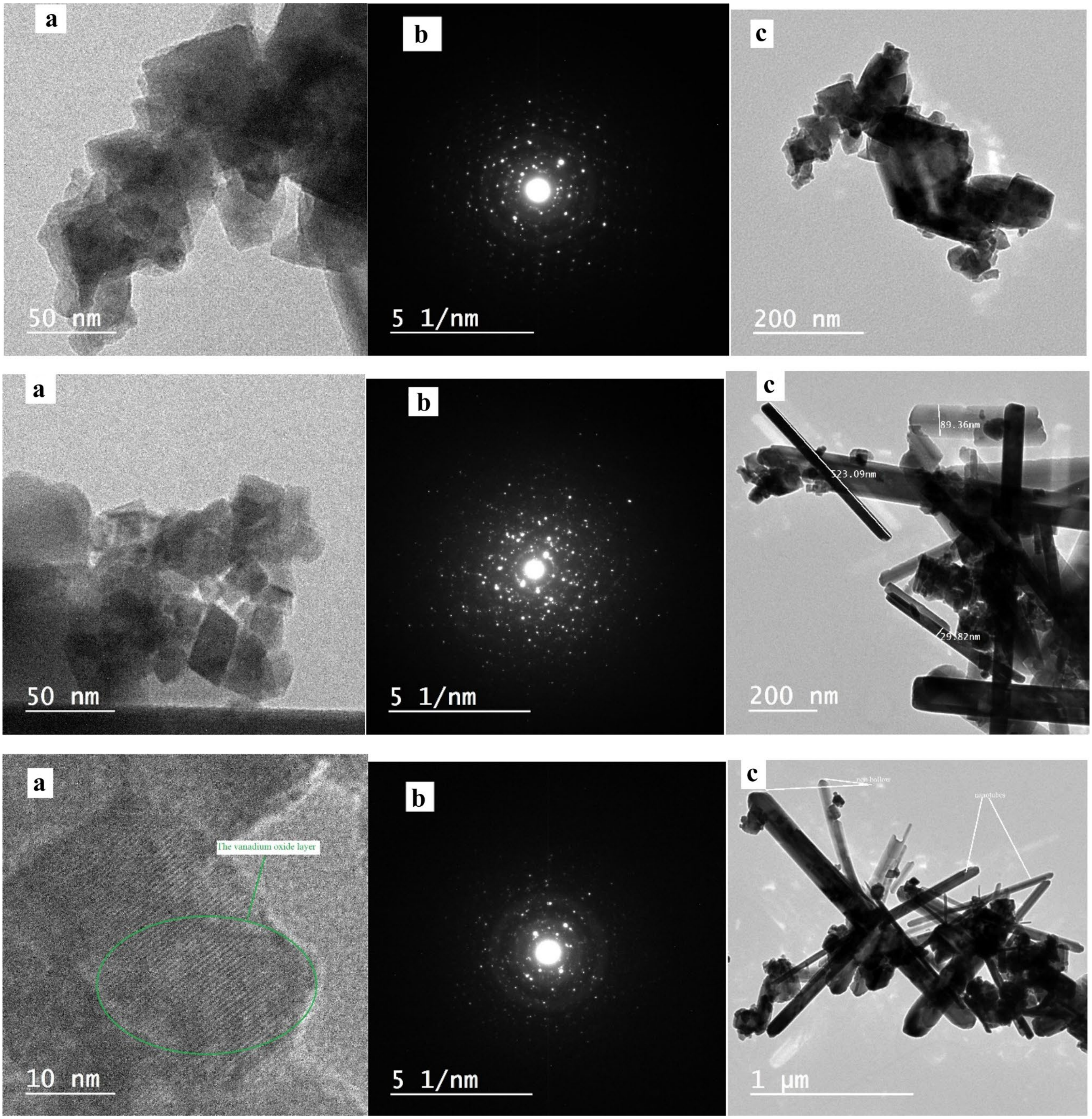

Fig. 12 **a** High-resolution TEM (HRTEM) of BSV glass system with different V_2O_5 content **b** Electron diffraction **c** TEM of BSV glass system with different V_2O_5

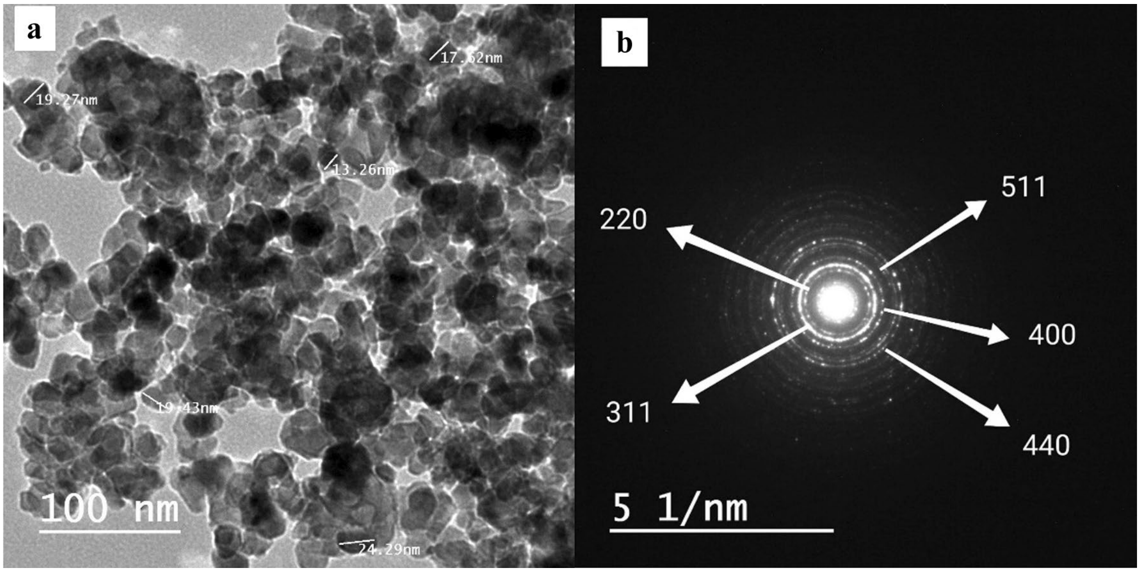

Fig. 13 **a** TEM micrograph of Nickel ferrite nanocrystal, **b** the electron diffraction image

Table 6 The change of Vanadium oxide nanorod, diameter, and the interplanar distance with V_2O_5 content

V_2O_5 content	Vanadium oxide rod nanorod (nm)	Diameter (nm)	Interplaner distance (nm)
0.1	64.17	41.57	8×10^{-3}
0.3	523.09	59.59	5.3×10^{-3}
0.5	930.21	76.67	6.1×10^{-3}

nanorods for low content V_2O_5. These results match the previous results of the work given by32.

The reaction of V_2O_5 with the glass matrix is observed from the TEM micrograph. The length and diameter of the rod depending on the condition of preparation. The maximum rod length that has been found is up to 0.93 µm.

The HRTEM is shown in Fig. 12a. The high-resolution images show the solid and nonhollow character. The layers that appear in the micrograph Fig. 12a contain vanadium oxide. The average interplanar distance between V_2O_5 layers gives rise to the corresponding reflection in the electron diffraction pattern shown in Fig. 12b. The interplanar distance for various V_2O_5 content was calculated and is presented in Table 6 33.

3.3.2 *TEM of* nickel *ferrite*

The TEM micrograph of Nickel ferrite nanocrystal and the electron diffraction image are shown in Fig. 12a, b.

The particle size, according to the TEM image, is found to be 23.67 nm. The particle size obtained from TEM images agrees with the size calculated from XRD 25.52 nm34.

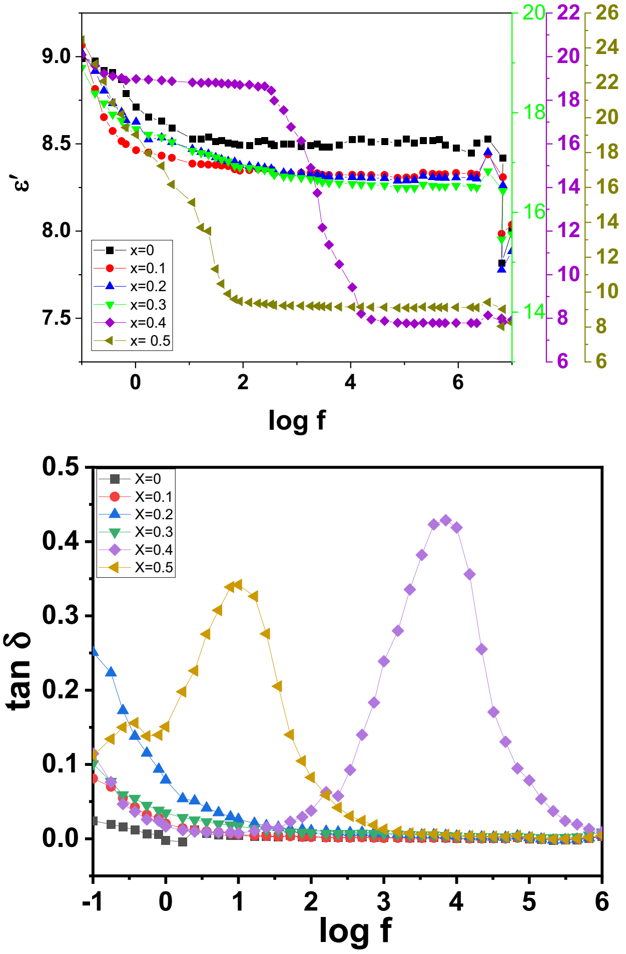

Fig. 14 The frequency dependence of real part ε′ and tan δ for the BSV glass system

Table 7 The value of dielectric constant ε′ at frequency 100 Hz and the value of tan δ at frequency 1 Hz and relaxation time ($\tau_{M''}$) with vanadium oxide content

V_2O_5 content	ε′	Tan δ	$\tau_{M''}$(sec)
0	18.2	0.01	0.064
0.1	18.3	0.02	0.048×10^{-6}
0.2	6	0.11	0.053
0.3	16.9	0.05	12.35×10^{-6}
0.4	18.3	0.01	10.51×10^{-3}
0.5	9.1	0.01	0.048×10^{-6}

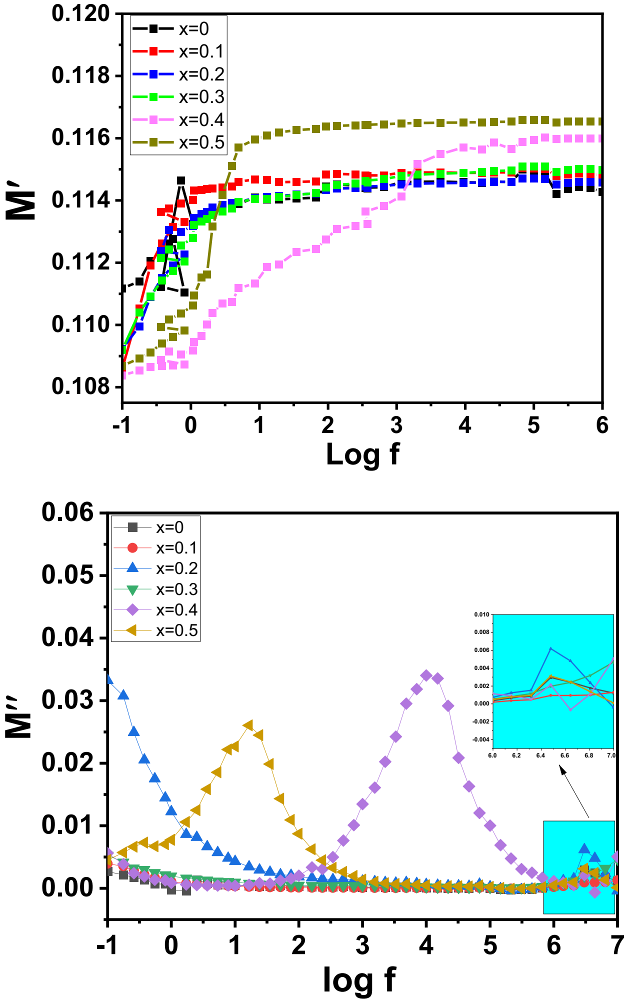

Fig. 15 The frequency dependence of M′ and M″ for BSV glass system

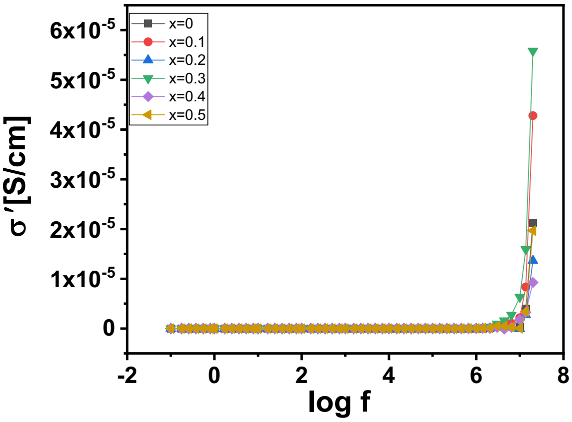

Fig. 16 The variation of AC conductivity σ′ with applied frequency at room temperature of BSV glass system

Table 8 The variation of AC conductivity σ′ of BSV glass system

V_2O_5 content	σ′ [S/cm]
0	22×10^{-6}
0.1	45×10^{-6}
0.3	55×10^{-6}
0.4	9×10^{-6}
0.5	2×10^{-5}

The electron diffraction pattern shows concentric rings in Fig. 13b, which matches well with the diffraction pattern plans of XRD. The electron diffraction selected area indicates that the nanoparticle prepared is crystalline, which is proved by the presence of different concentering rings as confirmed by XRD. The measured *d*-spacing from the electron diffraction image also matches the value obtained from XRD. The TEM image shows that the particles have an irregular shape Fig. 13a with some agglomeration.

3.4 Dielectric properties

3.4.1 Dielectric properties of BSV glass system

The glass system (0.5-x) wt.% B_2O_3 + (0.5) wt.% Sb_2O_3 + (x) wt.% V_2O_5 where x = (0, 0.1, 0.2, 0.3, 0.4 and 0.5) wt.% at different frequency and different V_2O_5 ratio encoded into BSV glass system. Figure 14 shows the variation of the dielectric constant ε', ε'' and dielectric loss tan δ as a function of logarithmic frequency, for different vanadium oxide content value x = 0, 0.1, 0.2, 0.3, 0.4 and 0.5 wt.%. content. It can be seen that the dielectric constant and dielectric loss gradually decrease with frequency. The ε' and dielectric loss has large values at low frequencies due to the high net polarization in which the hoping electron between different glass sites can follow the external electric field frequency. However, at high frequency, the charge carrier cannot successfully follow the frequency of the external field and lay behind, resulting in the decrease of dielectric constant and dielectric loss.

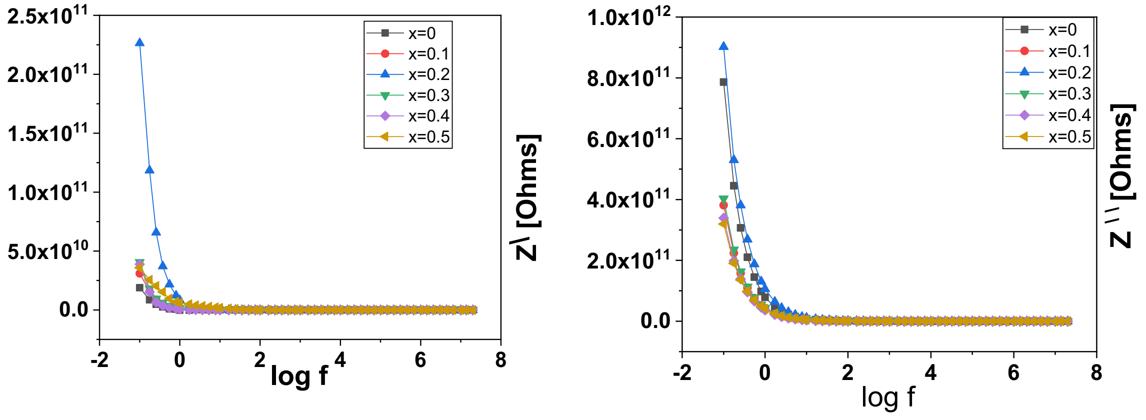

Fig. 17 The behavior of the real and imaginary part Z′ and Z″ for ac impedance respectively as a function of the frequency of BSV glass system

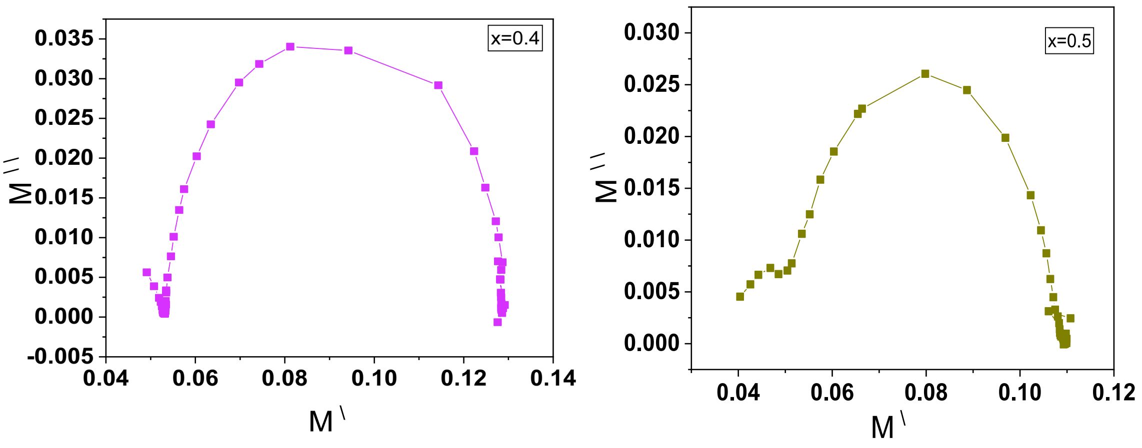

Fig. 18 Cole- Cole diagram of BSV glass system

The values of the dielectric constant ε' at frequency 100 Hz for all vanadium oxide content are decreasing with the increase of vanadium oxide content, whereas the value of tan δ at 1.0 HZ frequency shows an anomalous behavior at different vanadium oxide content as shown in Table 7. This behavior can be attributed to the decreased vacant site for hoping charge carriers in glass, leading to the variation of polarization and the values of dielectric constant and dielectric loss.

Modulus formalization of BSV glass system:

The electric modulus of glass is introduced to understand the bulk response of material as electrode polarization effect are monoamide the electric modulus is given from the equation35:

$$M^* = \frac{1}{\varepsilon^*} = M' + iM'' \tag{9}$$

where M' and M'' *the* real and imaginary parts of modulus. Figure 15 shows the frequency dependence of M' and M'' at various vanadium oxide content. It is observed that M' and M'' have the value near zero at low frequency. This is attributed to the negligible contribution of electrode polarization. With the increase in frequency M' increase gradually and a broch maximum value due to the relaxation process and the reduction of space charge effect.

It's observed that the relaxation peaks shift toward lower frequency by increasing vanadium oxide content, as shown in Table 7. Below the peak of M'' the ions derivate to long distances, and at frequencies above the peak, the ions are localized to a potential wall and only free to move in this wall. The relaxation time τ was calculated from the relation36:

$$\tau = \frac{1}{2\pi f_p} \tag{10}$$

AC conductivity of BSV glass system:

Figure 16 shows the frequency dependence of the glass system (50-x) $B_2O_3 + 50Sb_2O_3 + xV_2O_5$ where $x = 0,0.1,0.2,0.3,0.4$ and 0.5 at different frequencies and different V_2O_5 ratio.

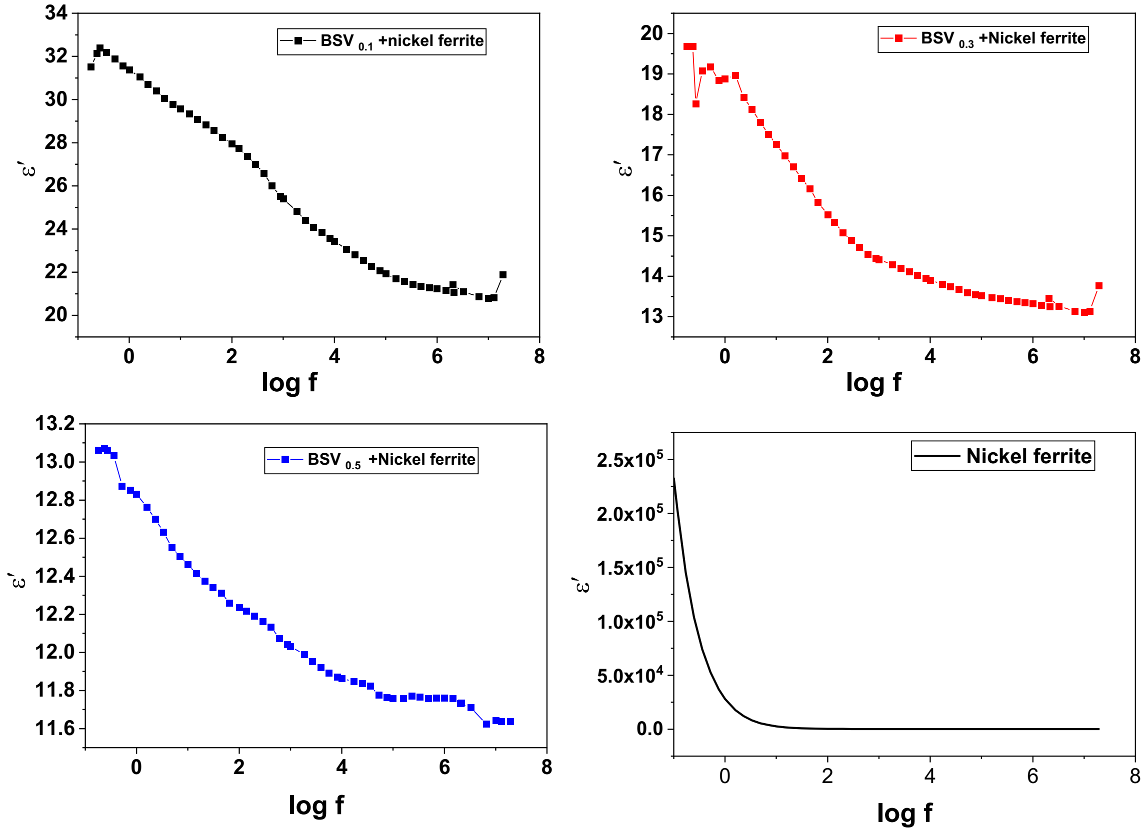

Fig. 19 Show the variation of real part of dielectric permittivity of glass composite with nickel ferrite and nickel ferrite

It is observed that the conductivity σ' increase with increasing frequency and vanadium oxide content up to $x = 0.3$ and then decrease. It is shown that the conductivity is high for high frequency, confirming the presence of a polearm hopping conduction mechanism. At high frequency, the conductivity is high due to the reduction of space charge polarization. At low frequencies, more and more charges accumulate at the interface between the electrode, leading to a drop in conductivity at that frequency range. The conductivity increase up to 0.3 may be due to the excess of electrons that contribute to the conduction mechanism from vanadium oxide. Above $x = 0.3$, the effect of polarization on the conductivity is the predominant factor that reduces the conductivity due to the scattering effect of hopping electrons12. At low frequency, the AC conductivity is constant, and after a specific frequency 10^7 Hz increases rapidly. This behavior is typical for the glass system and can be explained by Koop's and maxwell Wagner's model7. The composition dependence of ac conductivity is given in Table 8 at room temperature.

As the vanadium oxide increase, a large number of electric dipole moments appear, contributing to the polarization and reducing the conductivity above $x = 0.3$ 7.

The impedance of BSV glass system:

The behavior of the real and imaginary part Z' and Z'' for ac impedance respectively as a function of frequency shown in Fig. 17 for glass samples at different vanadium content. The complex ac impedance Z can be obtained from Z' and Z'' as the following equation37:

$$Z = Z' + iZ'' \tag{11}$$

As shown in Fig. 17, the values of $Z' + Z''$ are both very high at low frequency for all V_2O_5 content samples. These values begin to decrease as the frequency increases until it becomes constant at a high-frequency value. We can observe that the value of Z' increase by increasing V_2O_5 up to $x = 0.4$ and the decrease above that value.

The most important factor that affects impedance behavior is the microstructure factor. The real part Z' and imaginary part Z'' give information about the material's resistive and reactive parts respectively 37.

Cole–Cole diagram of BSV glass system:

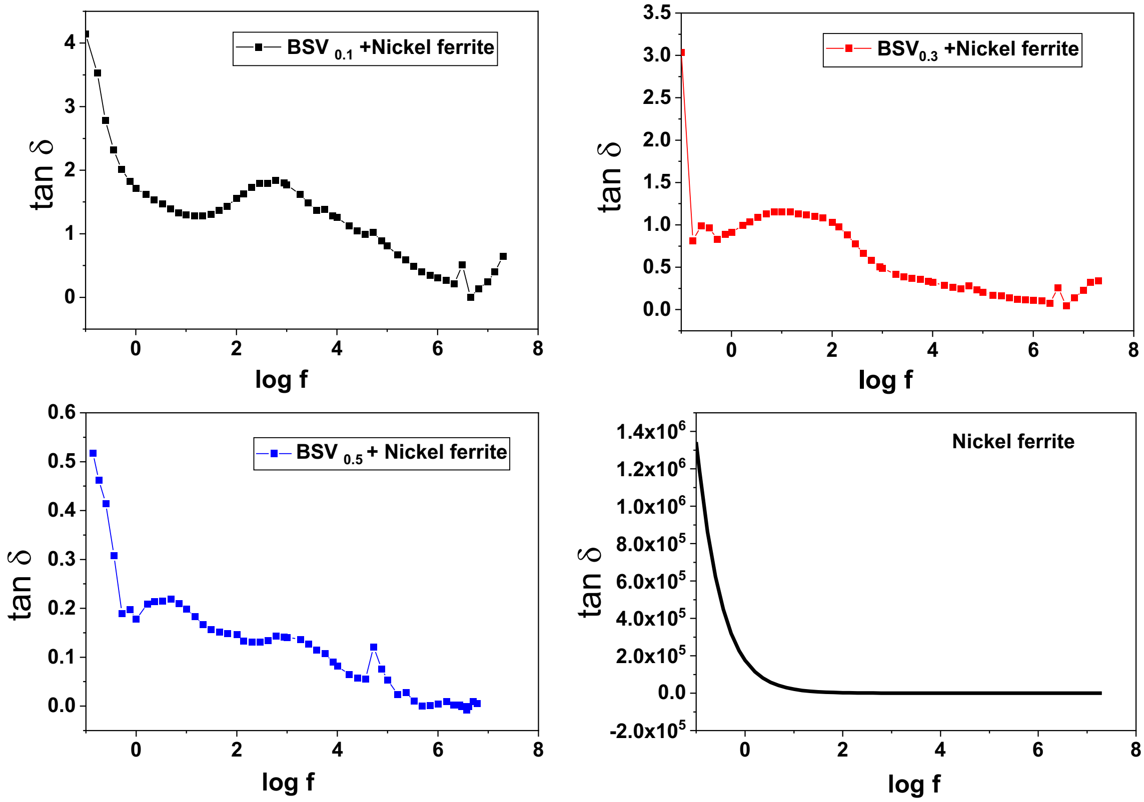

Fig. 20 Show the variation of dielectric loss of glass composite with nickel ferrite

Figure 18 shows the Cole–Cole plot of samples with $x = 0.4$ and 0.5, which gives two semicircles and obeys the non-Deby relaxation type. The double relaxation effect is due to the grain and grain boundary. The first and second circuits represent the grain boundary's resistance at low frequency and grain at high frequency, respectively.

3.4.2 Dielectric of BSV composite glass system

Figure 19 shows the variation of the real part of dielectric permittivity as a function of frequency for the glass samples (50-x) $B_2O_3 + 50Sb_2O_3 + xV_2O_5$ where $x = 0,0.1,0.2,0.3,0.4$ and 0.5 doped with a fixed content of ferrite weight percentage and at different V_2O_5 content. It can be seen that the dielectric constant and dielectric loss at low-frequency sharp decrease in their values.

In the presence of the hoping mechanism of ferrite, the dielectric behavior at low frequency depends on the fact that the charge carrier hops easily between the sites with low free energy, which increases the polarization, increases the dielectric constant, and increases dielectric loss values. On the other hand, at high frequency, the charge carrier cannot follow the external field frequency, which decreases polarization, dielectric constant, and dielectric loss values, as shown in Fig. 20.

The effect of ferrite addition to the glass matrix on dielectric constant and dielectric loss is controlled by the ratio between V_2O_5 content to ferrite content. At higher V_2O_5 / ferrite content, the dielectric constant increase compared to its value for the same sample without ferrite.

The presence of ferrite with a high concentration of Fe^{3+}–O–Fe^{3+} bond decreases the hopping process, and the charge carriers cannot follow the external electric field frequency. So, the dielectric constant values are small compared with the glass matrix without ferrite, especially for samples $x = 0.1$ and 0.3. It's observed that the sample $x = 0.5$ V_2O_5 content the dielectric constant has a high value compared with before ferrite addition. At high V_2O_5 $x = 0.5$ content, the interfacial polarization arises from the interaction between V_2O_5 and ferrite, giving rise to the interfacial polarization and dielectric constant.

Electrical modulus spectrum BSV glass with ferrite

The electrical modulus is introduced to justify the electrical relaxation behavior in the glass matrix samples containing ferrite; it is helpful to introduce the material's response as electrode polarization effects are minimized. The electric modulus is given by35:

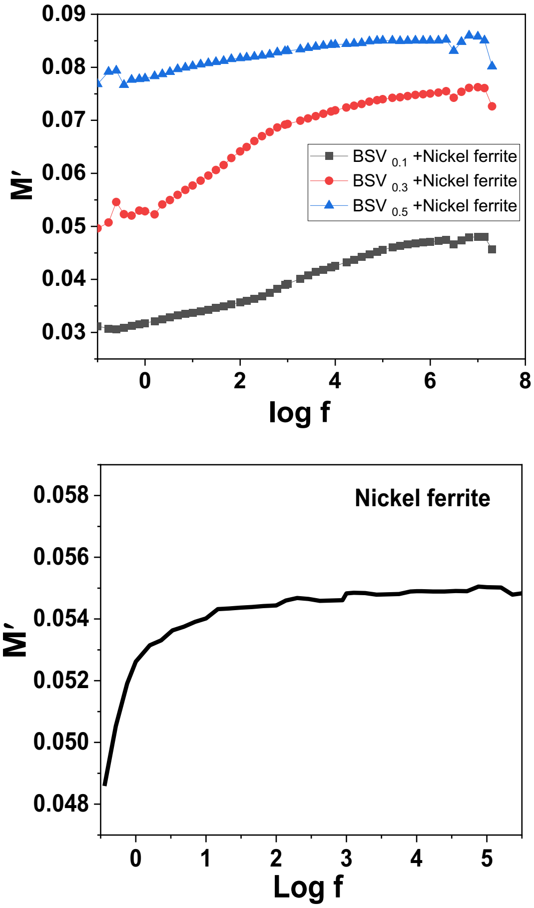

Fig. 21 Shows the frequency dependence of M′ for the glass samples containing ferrite and nickel ferrite

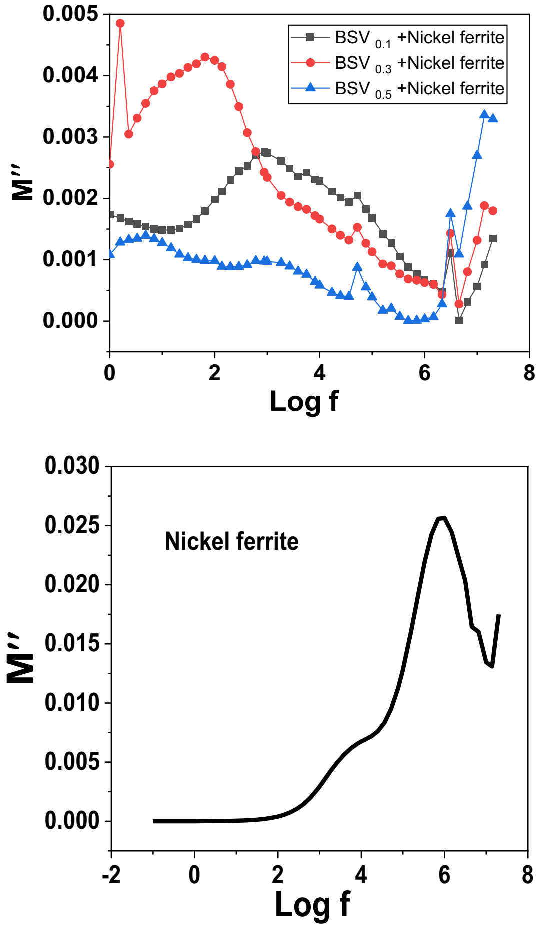

Fig. 22 Shows the frequency dependence of M″ for the glass samples containing ferrite and nickel ferrite

$$M^* = \frac{1}{\varepsilon^*} = M' + iM'' \tag{12}$$

where M' and M'' are real and imaginary parts of electrical modulus.

Figure 21 shows the frequency dependence of M' for the glass samples containing ferrite. It was noticed for glass samples without ferrite, the modulus at low frequency was nearly equal to zero, whereas for samples containing ferrites is not the same case at low frequency, which means that the M' has a higher value than zero. This may be attributed to the contribution of electrode polarization not negligible in ferrite's presence. At higher frequency M' increase and approach maximum value due to the reduction of space charge effect.

The imaginary part of the modulus M'' is shown in Fig. 22. Similar nature of frequency dependence of M'' All glass samples were observed with the relaxation peak shift to the lower frequency site.

The relaxation peak frequency was shifted to the lower frequency, so the relaxation time increased by increasing V_2O_5 in the presence of ferrite. The relaxation time was calculated from8, 38:

$\tau = \frac{1}{2\pi f_p}$ (13).Where f_p is peak frequency, and given in Table 9.

Table 9 The relaxation time for BSV glass composite with ferrite

V_2O_5 content	$\tau_{M''}$(sec)
0.1	2.15×10^{-3}
0.3	1.63×10^{-4}
0.5	30.3×10^{-3}

AC conductivity:

The variation of AC conductivity σ' with applied frequency at room temperature shown in Fig. 23. The ferrite samples σ'_{ac} increases linearly with the applied frequency tending to the increase of charge carriers hoping mechanism between different localized sites helping the charge

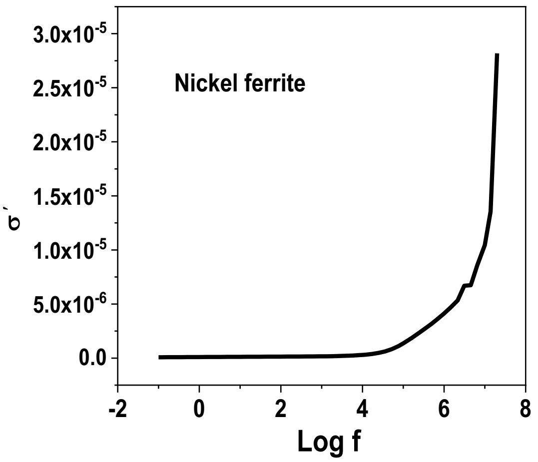

Fig. 23 The variation of AC conductivity σ′ with applied frequency at room temperature of nickel ferrite nanoparticle

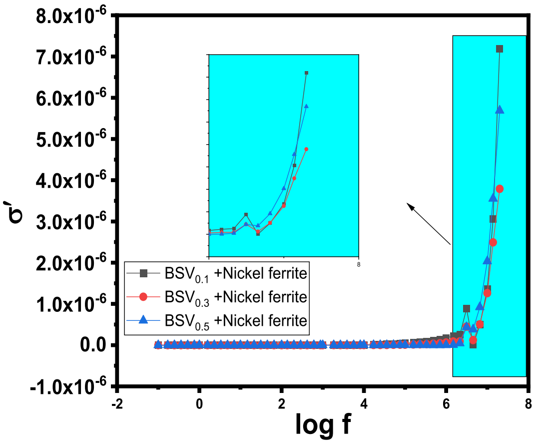

Fig. 24 Shows the frequency dependence with the conductivity of the glass system BSV doped with a fixed content of ferrite weight percentage and at different V_2O_5 content

carrier to liberate from its trapping centers leading to the increase of conductivity at high frequency.

Ac conductivity of BSV glass with ferrite:

The real σ'_{ac} part of ac conductivity of the borate glass sample (50-*x*) $B_2O_3 + 50Sb_2O_3 + xV_2O_5$ where $x = 0,0.1,0.2,0.3,0.4$ and 0.5 doped with fixed content o.

ferrite weight percentage and at different V_2O_5 content coated by silver paste at the surface is shown in Fig. 24 as a function of frequency logf in the range between 10 MHz at different V_2O_5 content. The value of σ' is very small at low frequencies for all samples with different V_2O_5 content. The σ' start to increase at a certain frequency of 3.98×10^6 HZ due to the increase of space charge polarization12, 24. We also observed that the values of σ' is increased as V_2O_5 content increase from 3.05 to 5.62 when V_2O_5 content increases from 0.1 to 0.5.

The plateau behavior of σ' at low frequency gives rise to dc conductivity arising from the hoping electrons between the localized sites (octahedral and tetrahedral of ferrite) according to the equation13, 39:

$$\sigma^*_{total} = \sigma_{dc} + \sigma_{ac}(\omega)^n \quad (14).$$

where σ_{dc}: dc conductivity and $\sigma_{ac}(\omega)^n$ frequency dependence of ac conductivity.Whereas, at high-frequency σ shows frequency dependence which gives rise to ac conductivity according to the power low $\sigma_{ac}(\omega) = A\,\omega^n$ where A is the constant dependence of the value of V_2O_5 content and n is the frequency exponent37. In the high-frequency region, some dispersion was observed, which is predominant in this frequency range.

The AC impedance **Z′** and **Z″** of BSV glass with ferrite:

The real and imaginary part Z' and Z'' of the impedance of the studied borate glass samples doped with 0.05 gm nickel ferrite was measured at a frequency range from 0.1 HZ to 10MHZ at different V_2O_5 content were shown in Fig. 25. The ac impedance can be obtained from the following equation13, 40:

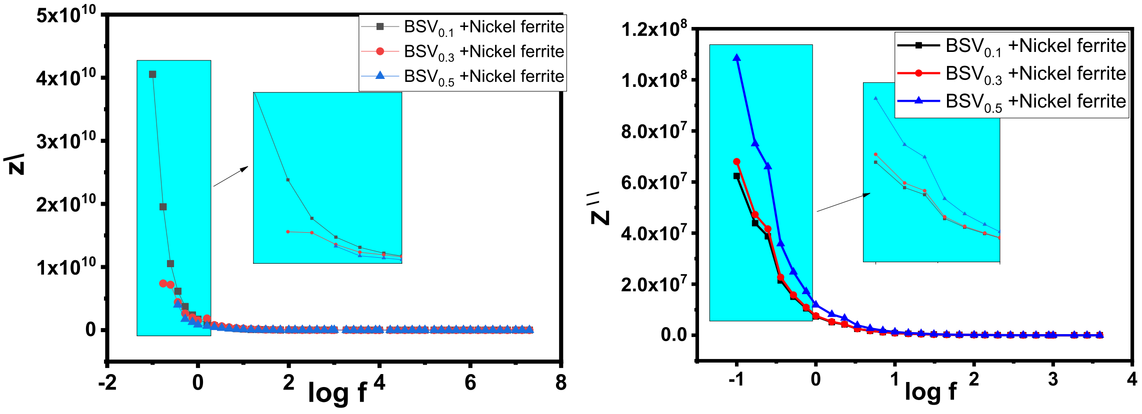

Fig. 25 Show the AC impedance Z′ and Z″ of BSV glass with ferrite

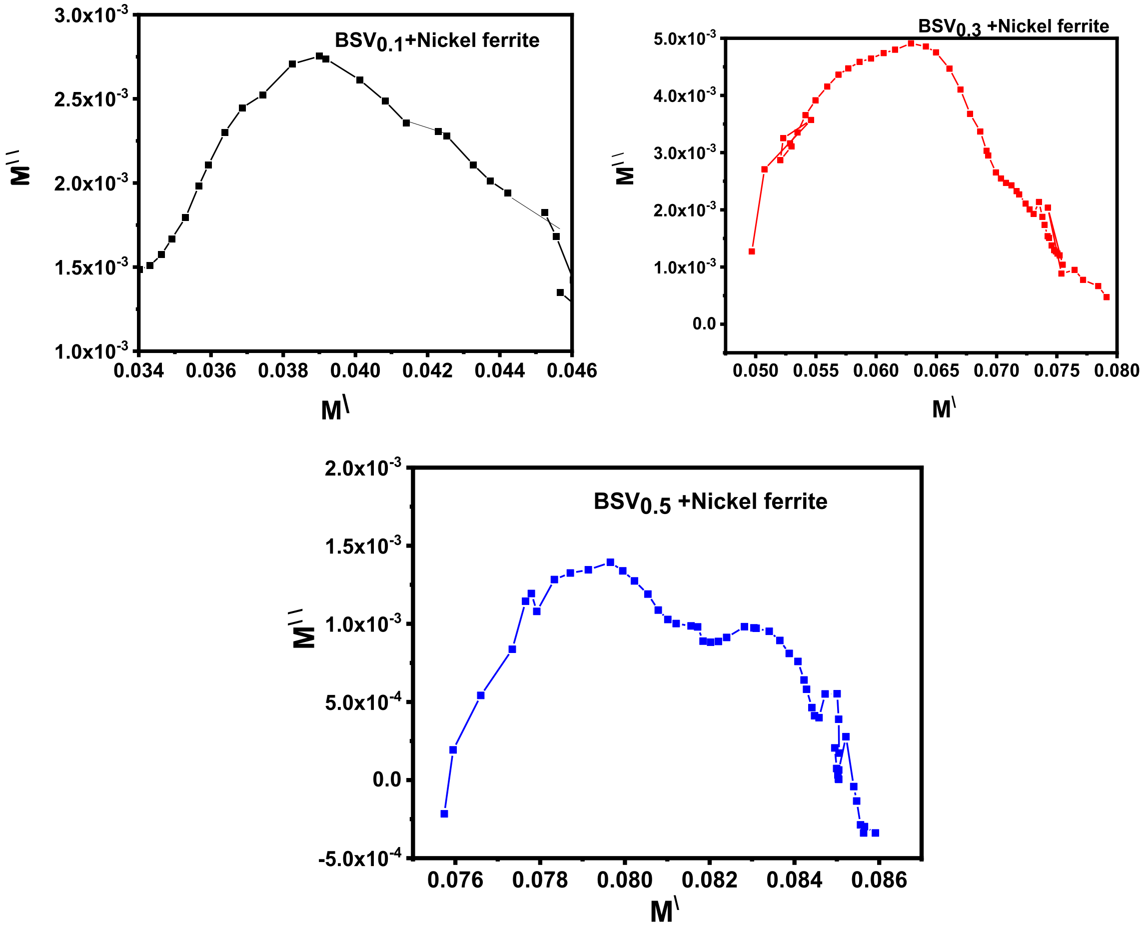

Fig. 26 Cole–Cole diagram of BSV composite glass system

$$Z^{*} = Z' + iZ'' \tag{15}$$

The values of Z' and Z'' are both high at low frequency for all samples, and these values at high frequency start to decrease until they constantly reach very high frequency. We can observe that the value of Z' and Z'' at low-frequency decrease by increasing V_2O_5 content from 4×10^{10} to 0.7×10^{10} when V_2O_5 changes from 0.1 to 0.5-mol percent %.

Cole–Cole diagram

The plot of M' and M'' in borate glass can be classified as debay type and nondebay type as shown in Fig. 26. The relaxation is Deby type if the semicircular is formed whose center is laying on the real axis and non-Deby type if the semicircular is deformed as in our case. The semicircular is obtained with the shape that the center has deviated from the axis, and hence our relaxation process is attributed to the non-Deby type.

Generally, the non-Deby type is atypical behavior of the amorphous glass due to the random distribution of the charge carriers in the glass matrix. The Cole–Cole diagram for the borate glass sample with different V_2O_5 content is different in shape and behavior due to the change of relaxation frequency for the other samples.

4 Conclusion

BSV glass system, nickel ferrite, and BSV composite system are prepared. These glasses show that the V_2O_5 nanoparticle was grown inside the borate glass matrix homogenous in the form of nanorods. It's shown that the relaxation peaks shift toward lower frequency, and the conductivity increase by increasing vanadium oxide content in the BSV glass system. According to the Cole–Cole diagram of the BSV glass system gives two semicircles obeying what is called the non-Deby relaxation type. In BSV composite glass, the dielectric constant increases compared with its value for the same sample without ferrite. The presence of ferrite with a high concentration of Fe^{3+}–O–Fe^{3+} bond decreases the hopping process and the charge carriers cannot follow the external electric field frequency. So, the dielectric constant values are small compared with that for glass matrix without ferrite. FTIR provides different functional groups found in the BSV glass system, and the spectra show a similar functional group as the BSV glass system in addition to the two characteristic bands that appeared in the far infrared region, which are assigned to octahedral and tetrahedral group complex for Fe^{3+}–O^{2-}. In this paper, we found that adding vanadium oxide to the glass matrix is a very effective parameter since it shows the growing process inside the glass matrix by increasing the adding ratio of V_2O_5. The comparison between BSV glass and BSV composite glass shows a difference in dielectric constant, which clears the difference in the structure of the glass and composite system.

Acknowledgements The research funding from the Ministry of Science and Higher Education of the Russian Federation (Ural Federal University Program of Development within the Priority-2030 Program) is gratefully acknowledged.

Declarations

Conflict of interests The authors declare that they have no known competing financial interests or personal relationships that could have appeared to influence the work reported in this paper.

References

1. R.K. Singh, A. Srinivasan, Bioactivity of ferrimagnetic MgO-CaO-SiO2-P2O5-Fe2O3 glass-ceramics. Ceram. Int. **36**(1), 283–290 (2010). https://doi.org/10.1016/j.ceramint.2009.07.028
2. H.I. Hsiang, T.H. Chen, Electrical properties of low-temperature-fired ferrite-dielectric composites. Ceram. Int. **35**(5), 2035–2039 (2009). https://doi.org/10.1016/j.ceramint.2008.11.004
3. K.S. Kim, S.H. Shim, S. Kim, S.O. Yoon, Low temperature and microwave dielectric properties of TiO2/ZBS glass composites. Ceram. Int. **36**(5), 1571–1575 (2010). https://doi.org/10.1016/j.ceramint.2010.02.030
4. L. Zhou, H. Lin, W. Chen, L. Luo, IR and Raman investigation on the structure of (100–x)B2O3-x [0.5 BaO-0.5 ZnO] glasses. J. Phys. Chem. Solids **69**(10), 2499–2502 (2008). https://doi.org/10.1016/j.jpcs.2008.05.013
5. G. Srinivasarao, N. Veeraiah, The role of iron ions on the structure and certain physical properties of PbO-As2O3 glasses. J. Phys. Chem. Solids **63**(4), 705–717 (2002). https://doi.org/10.1016/S0022-3697(01)00218-9
6. T.A. Taha, A.A. Azab, E.H. El-Khawas, Comprehensive study of structural, magnetic and dielectric properties of borate/Fe3O4 Glass nanocomposites. J. Electron. Mater. **49**(2), 1161–1166 (2020). https://doi.org/10.1007/s11664-019-07825-z
7. A.S. Abouhaswa, Y.S. Rammah, S.E. Ibrahim, A.A. El-Hamalawy, Structural, optical, and electrical characterization of borate glasses doped with SnO2. J. Non. Cryst. Solids **494**(March), 59–65 (2018). https://doi.org/10.1016/j.jnoncrysol.2018.04.051
8. Y. Gandhi, N. Purnachand, K.S.V. Sudhakar, T. Satyanarayana, N. Veeraiah, Influence of modifier oxides on some physical properties of antimony borate glass system doped with V2O5. Mater. Chem. Phys. **120**(1), 89–97 (2010). https://doi.org/10.1016/j.matchemphys.2009.10.026
9. T. Prabhakaran, J. Hemalatha, Combustion synthesis and characterization of highly crystalline single phase nickel ferrite nanoparticles. J. Alloys Compd. **509**(25), 7071–7077 (2011). https://doi.org/10.1016/j.jallcom.2011.03.176
10. A. Alarifi, N.M. Deraz, S. Shaban, Structural, morphological and magnetic properties of NiFe2O4 nano-particles. J. Alloys Compd. **486**(1–2), 501–506 (2009). https://doi.org/10.1016/j.jallcom.2009.06.192
11. J. Huo, M. Wei, Characterization and magnetic properties of nanocrystalline nickel ferrite synthesized by hydrothermal method. Mater. Lett. **63**(13–14), 1183–1184 (2009). https://doi.org/10.1016/j.matlet.2009.02.024
12. D. Shajan, P. Murugasen, S. Sagadevan, Analysis on the structural, spectroscopic, and dielectric properties of borate glass. Dig. J. Nanomater. Biostruct. **11**(1), 177–183 (2016)
13. N. Atef, G. El Damrawi, A. Hassan, L.S. El-Deen, Dielectric Studies on CuO-Na₂O-B₂O₃ Glasses. New J. Glas. Ceram. **10**(04), 45–56 (2020). https://doi.org/10.4236/njgc.2020.104004
14. S. Joshi, M. Kumar, S. Chhoker, G. Srivastava, M. Jewariya, V.N. Singh, Structural, magnetic, dielectric and optical properties of nickel ferrite nanoparticles synthesized by co-precipitation method. J. Mol. Struct. **1076**, 55–62 (2014). https://doi.org/10.1016/j.molstruc.2014.07.048
15. A. Kaaouass, A. Ben Ali, F. Alloun, A. Zarrouk, M. Saadi, Structural, thermal and physical properties of the calcium borovanadate glasses belonging to the 40CaO-(60–x)B2O3-xV2O5 system. Biointerface Res. Appl. Chem. (2022). https://doi.org/10.33263/BRIAC131.048
16. Y.A. Alibwaini et al., Synthesis, characterizations, optical and photoluminescence properties of polymer blend PVA/PEG films doped eosin Y (EY) dye. Opt. Mater. (Amst) **111**(August), 2020 (2021). https://doi.org/10.1016/j.optmat.2020.110600
17. N. Laorodphan, P. Pooddee, P. Kidkhunthod, P. Kunthadee, W. Tapala, R. Puntharod, Boron and pentavalent vanadium local environments in binary vanadium borate glasses. J. Non. Cryst. Solids **453**, 118–124 (2016). https://doi.org/10.1016/j.jnoncrysol.2016.10.005
18. C. Gautam, A.K. Yadav, A.K. Singh, A review on infrared spectroscopy of borate glasses with effects of different additives. ISRN Ceram. **2012**, 1–17 (2012). https://doi.org/10.5402/2012/428497
19. T.D. Abdelaziz, F.M. Ezzeldin, H.A. El Batal, A.M. Abdelghany, Optical and FT Infrared spectral studies of vanadium ions in cadmium borate glass and effects of gamma irradiation. Spectrochim. Acta Part A Mol Biomol. Spectrosc. **131**, 497–501 (2014). https://doi.org/10.1016/j.saa.2014.04.035
20. V. Kundu, R.L. Dhiman, A.S. Maan, D.R. Goyal, Structural and physical properties of Fe2O3-B2O3-V2O5 glasses. Adv. Condens. Matter Phys. **2008**, 1–7 (2008). https://doi.org/10.1155/2008/937054
21. A.M. Abdelghany, A.H. Hammad, Impact of vanadium ions in barium borate glass. Spectrochim. Acta Part A Mol. Biomol. Spectrosc. **137**, 39–44 (2015). https://doi.org/10.1016/j.saa.2014.08.012
22. E.A. Abdel Wahab, K.S. Shaaban, R. Elsaman, E.S. Yousef, Radiation shielding and physical properties of lead borate glass-doped ZrO2 nanoparticles. Appl. Phys. A Mater. Sci. Process. **125**(12), 1–15 (2019). https://doi.org/10.1007/s00339-019-3166-8
23. S.K. Arya, G. Kaur, K. Singh, Effect of vanadium on the optical and physical properties of lithium borate glasses. J. Non. Cryst. Solids **432**, 393–398 (2016). https://doi.org/10.1016/j.jnoncrysol.2015.10.037

24. R.A. Elsad, A.M. Abdel-Aziz, E.M. Ahmed, Y.S. Rammah, F.I. El-Agawany, M.S. Shams, FT-IR, ultrasonic and dielectric characteristics of neodymium (III)/ erbium (III) lead-borate glasses: experimental studies. J. Mater. Res. Technol. **13**, 1363–1373 (2021). https://doi.org/10.1016/j.jmrt.2021.05.029
25. R. Sridhar, D. Ravinder, K.V. Kumar, Synthesis and characterization of copper substituted nickel nano-ferrites by citrate-gel technique. Adv. Mater. Phys. Chem. **02**(03), 192–199 (2012). https://doi.org/10.4236/ampc.2012.23029
26. Y. Ahn, E.J. Choi, S. Kim, H.N. Ok, Magnetization and Mössbauer study of cobalt ferrite particles from nanophase cobalt iron carbonate. Mater. Lett. **50**(1), 47–52 (2001). https://doi.org/10.1016/S0167-577X(00)00412-2
27. J.Y.C. Sun, Foundry technology trend. Microelectron. Manuf. Yield Reliab. Fail. Anal. **3510**, 19 (1998). https://doi.org/10.1117/12.324380
28. S. Balaji, R.K. Selvan, L.J. Berchmans, S. Angappan, K. Subramanian, C.O. Augustin, Combustion synthesis and characterization of Sn4+ substituted nanocrystalline NiFe2O4. Mater. Sci. Eng. B Solid-State Mater. Adv. Technol. **119**(2), 119–124 (2005). https://doi.org/10.1016/j.mseb.2005.01.021
29. A. Rais, K. Taibi, A. Addou, A. Zanoun, Y. Al-Douri, Copper substitution effect on the structural properties of nickel ferrites. Ceram. Int. **40**(9), 14413–14419 (2014). https://doi.org/10.1016/j.ceramint.2014.06.037
30. H.A. ElBatal, M.Y. Hassaan, M.A. Fanny, M.M. Ibrahim, Optical and FT infrared absorption spectra of soda lime silicate glasses containing nano Fe2O3 and effects of gamma irradiation. SILICON **9**(4), 511–517 (2017). https://doi.org/10.1007/s12633-014-9262-7
31. F.H. ElBatal, A.M. Abdelghany, F.M. Ezz ElDin, H.A. ElBatal, Vanadium structural role in binary fluoride borate glasses and effects of gamma irradiation. Radiat. Phys. Chem. **1**, 2 (2020). https://doi.org/10.1016/j.radphyschem.2019.108659
32. S. Joshi, R. Arindom, T. Dikshit, B. Anish, A.G. Deep, P. Pallav, Conceptual paper on factors affecting the attitude of senior citizens towards purchase of smartphones. Indian J. Sci. Technol. **8**(12), 83–89 (2015). https://doi.org/10.17485/ijst/2015/v8i
33. E. Kianfar, Recent advances in synthesis, properties, and applications of vanadium oxide nanotube. Microchem. J. **145**, 966–978 (2019). https://doi.org/10.1016/j.microc.2018.12.008
34. S. Debnath, A. Das, R. Das, Effect of cobalt doping on structural parameters, cation distribution and magnetic properties of nickel ferrite nanocrystals. Ceram. Int. **47**(12), 16467–16482 (2021). https://doi.org/10.1016/j.ceramint.2021.02.095
35. R.S. Gedam, D.D. Ramteke, Electrical, dielectric and optical properties of La2O 3 doped lithium borate glasses. J. Phys. Chem. Solids **74**(7), 1039–1044 (2013). https://doi.org/10.1016/j.jpcs.2013.03.001
36. S.G. Motke, S.P. Yawale, S.S. Yawale, Infrared spectra of zinc doped lead borate glasses. Bull. Mater. Sci. **25**(1), 75–78 (2002). https://doi.org/10.1007/BF02704599
37. A.A. Menazea, A.M. Abdelghany, N.A. Hakeem, W.H. Osman, F.H. Abd El-kader, Precipitation of silver nanoparticles in borate glasses by 1064 nm Nd:YAG nanosecond laser pulses: characterization and dielectric studies. J. Electron. Mater. **49**(1), 826–832 (2020). https://doi.org/10.1007/s11664-019-07736-z
38. B. Na, B. Tio, and L. P. Ceramics, "Piezoelectric and Dielectric Properties of Bi 2 O 3 -Doped," vol. 372, no. 20, pp. 1915–1918, 2008, doi: https://doi.org/10.5897/IJPS2015.
39. "glasses," pp. 1–16.
40. K.H. Mahmoud, F.M. Abdel-Rahim, K. Atef, Y.B. Saddeek, Dielectric dispersion in lithium-bismuth-borate glasses. Curr. Appl. Phys. **11**(1), 55–60 (2011). https://doi.org/10.1016/j.cap.2010.06.018